

Thermoelectric performance of higher manganese silicide nanocomposites



M. Saleemi ^{a,*}, A. Famengo ^b, S. Fiameni ^b, S. Boldrini ^b, S. Battiston ^b, M. Johnsson ^c, M. Muhammed ^a, M.S. Toprak ^{a,*}

^a Department of Materials and Nano Physics, KTH Royal Institute of Technology, Kista, Stockholm, Sweden

^b CNR, Institute for Energetics and Interphases (IENI-CNR), Corso Stati Uniti 4, I-35127 Padua, Italy

^c Department of Materials and Environmental Chemistry, Stockholm University, Stockholm, Sweden

ARTICLE INFO

Article history:

Received 24 July 2014

Received in revised form 29 August 2014

Accepted 1 September 2014

Available online 16 September 2014

Keywords:

Thermoelectrics

Higher manganese silicide

Spark plasma sintering

Nanostructured

ABSTRACT

Higher manganese silicides (HMS) are proven to be promising candidates as p-type thermoelectric material in the temperature range of 400–700 K. In this work, a series of nanostructured (NS) bulk MnSi_{1.73} with different levels of Ytterbium inclusions were fabricated via ball milling and the solid state reaction was completed by spark plasma sintering (SPS). Nanopowders and SPS consolidated Yb–HMS nanocomposites (NC) were characterized by X-ray diffraction (XRD) and scanning electron microscopy (SEM) to reveal the crystal structure and morphology respectively. High resolution transmission electron microscopy (HRTEM) coupled with energy dispersive X-ray spectroscopy (EDS) was used to investigate the material composition in bulk grains. Yb was observed to stay as nanoinclusions at the grain boundaries. TE transport properties, including Seebeck coefficient, electrical resistivity, and thermal diffusivity as well as charge carrier concentrations were evaluated. Thermal conductivity decreased with increasing Yb content, while the electrical conductivity improved for the highest Yb content. A highest figure of merit (ZT) of 0.42 at 600 °C was achieved for 1% Yb–HMS NC sample.

© 2014 Elsevier B.V. All rights reserved.

1. Introduction

High fuel prices and extensive consumption of the fossil fuels are hauling this world through imminent energy crisis. Thermoelectric generators (TEGs) may play a key role to meet this challenge as they can produce electricity from waste heat sources, including cars and various industries [1]. For instance, TEGs in car exhaust pipes with a conversion efficiency of 10–15% will reduce the fuel consumption by around 3–6%, which is potentially significant to meet the 2020 carbon emission goal for the car industry [2]. Thermoelectric (TE) materials are widely explored and their efficiency is defined by the dimensionless figure of merit, $ZT = \frac{S^2}{\rho\kappa}T$, where S is the Seebeck coefficient, ρ is the electrical resistivity, κ is the thermal conductivity, that is the sum of electronic (κ_e) and lattice (κ_l) conductivity contributions and T is the absolute temperature [3]. Acquiring high ZT value is often challenging due to the interdependence of these physical parameters. Many groups reported on the possibility of enhancing power factor (S^2/ρ) and reduced thermal conductivity with multiple nano-engineering approaches [4–9].

TE materials are categorized depending upon their application temperature range; chalcogenides are effective at low temperature (below 250 °C), skutterudites are promising at intermediate temperature (up to 500 °C) [10], and in case of high temperature (more than 600 °C) half-Heusler compounds, and transition metal oxides are representative examples [11]. Although these TE materials showed improved performance, they cannot dominate the TE market because most of their constituents are toxic, less abundant and/or very expensive [12]. This may hinder their further implementation for mass production. Silicide based materials are considered as the best candidate for mid to high temperature TE applications (400–600 °C) as their constituents are highly abundant, inexpensive, non-toxic and maintain a high stability [13]. Higher manganese silicides (HMS) are represented by MnSi_{2-x}, MnSi_{1.75} and MnSi_{1.8} compositions. They consist of a homologous series of crystallographically distinct phases referred to as the Nowotny Chimney Ladder phases. Four distinct phases of HMS have been reported with the atomic positions determined by XRD: Mn₄Si₇, Mn₁₁Si₁₉, Mn₁₅Si₂₆ and Mn₂₇Si₄₇ [14]. HMS are semiconductors with band gap energy from 0.4 eV to 0.7 eV [15]. They possess good TE properties and a maximum ZT 0.6 at 725 K have been reported by Gelbstein and co-workers [16].

* Corresponding authors.

Introduction of metallic inclusions may enhance the TE performance of HMS compounds. Electron and phonon collisions at the surface of the embedded particles significantly shortens their effective mean free path that may enhance the electrical properties and reduces the thermal conductivity [17]. Currently, there is not a single existing model that can describe the heat transport through composite materials containing dispersed metallic particles. Yamada et al. reported on iron and sodium added HMS samples and achieved a *ZT* of 0.31 at 800 K [18]. However, few results have been focusing on the partial substitution of Si by other elements to enhance the power factor. Luo et al. reported that substitution of Si by Al enhanced the figure of merit by 40% compared to undoped HMS samples [19]. Though, the thermal conductivity of such samples has not been reduced significantly. Similar claims were published by Ponnambalam et al. that Cr substituted MnSi_{1.73} sample has raised the *ZT* about 42% as compared to undoped MnSi_{1.73} [20]. Conventionally, HMS is fabricated through expensive and long term melting techniques to obtain the desired composition and crystal phases.

The goal of this work is the synthesis and detailed characterization of densely packed HMS nanocomposites (NC) containing Ytterbium (Yb), i.e. Yb-HMS composites. Yb is mainly used as a dopant of stainless steel or active laser media. Rare-earth elements, including Yb, have been observed to improve the performance of some other thermoelectric compounds [21], which is the reason for our choice of dopant for HMS. To the best of our knowledge there is no previous report about rare earth metal inclusions in HMS systems to date. In this work we have utilized ball milling (BM) and spark plasma sintering (SPS) to prepare and consolidate HMS and their Yb nanocomposites.

2. Experimental

Yb-HMS NCs were synthesized from 325 mesh silicon (Si) with 99.999% purity, manganese (Mn) powder with 99.95% purity obtained from Alfa Aesar and Yb chips with 99.99% purity from Sigma Aldrich was used. Each element was weighed under Argon, in glove box and loaded into tungsten carbide (WC) jar and balls with hexane as dispersion media for BM. Si to Mn molar ratio was 1.73 and 0.5 wt% and 1.0 wt% Yb metal content were used for two NC samples. Planetary BM with a speed of 400 rpm was performed for 8 h. Afterwards, powder was collected and dried at room temperature in the glove box to remove the excess solvent. Subsequently, the SPS compaction was carried out by using a Dr. Sinter 2050 setup, where all the compacts were made from powders filled in a graphite die having diameter of 15 mm, using optimized SPS conditions as described in our earlier work [22]. All the samples were sintered at 950 °C for 5 min holding time at an applied pressure of 75 MPa. After sintering, the samples were polished in order to remove the graphite layer.

2.1. Characterization

HMS crystal phases were identified by X-ray diffraction (XRD) utilizing Panalytical diffractometer (operated at 45 kV and 40 A) with a Cu K α source, wavelength 1.543 Å. Rietveld refinement of the XRD profiles was performed by the MAUD program for quantitative phase analysis, determination of crystallite sizes, and to obtain the theoretical densities of the compacted pellets (employing only the revealed crystallographic phases). Pellet densities were estimated via geometrical measurements. Morphology and composition of the samples were evaluated by performing field-emission scanning electron microscopy (FE-SEM) equipped with an Oxford energy-dispersive spectroscopy (EDS) setup. Focused ion beam (FIB) SEM was used to prepare the transmission electron microscopy (TEM) sample. HRTEM analysis was carried out by Philips TM30 TEM with an accelerating voltage of 200 keV, mapping and elemental composition analysis was performed with coupled EDS detector. SPS compacted sample was ground and particles were dispersed in ethanol which was then dropcast on the TEM grids to prepare HRTEM sample.

Thermal diffusivity was measured by a laser flash apparatus from Netzsch (LFA 457 MicroFlash) while thermal conductivity (κ) was calculated from the equation, $\kappa = \alpha \rho C_p$, where α is the thermal diffusivity, ρ is the bulk density and C_p is the specific heat of the material. The specific heat capacity was calculated by means of Netzsch Proteus analysis software, comparing the samples against the standard material Netzsch Pyroceram 9606. The Seebeck coefficient and electrical resistivity were measured from room temperature (RT) to 600 °C using an in house built apparatus described in details elsewhere [23]. All measurements were carried out under Ar atmosphere.

3. Results and discussion

Fig. 1 shows XRD patterns of BM samples from pure HMS and NCs. The results indicate the presence of only MnSi, Mn and Si phases and similar observations were stated also in other reports after the BM step [24,25]. It is difficult to distinguish between all the distinct crystallographic phases and these structures differ only by the *c*-axis, which is in all cases very long, compared to the *a*-axis [26]. Pure HMS BM sample phase contents were identified as 51 wt% HMS, 22 wt% MnSi, 12 wt% Si and 14 wt% Mn from Rietveld fitting data. Sadia et al. reported optimized ball milling parameters: they concluded that increase of milling time will not facilitate formation of more HMS phase [25], instead it possibly increases the metallic content of MnSi, which is detrimental for the TE performance [24]. **Fig. 1(b and c)** are the XRD patterns of Yb-HMS NCs: Yb peaks (ICSD # 43585) were not observed since the Yb content is close to the detection limit of the lab XRD tool. **Fig. 2** displays the XRD patterns of SPS compacted sample where all major characteristic peaks of pure HMS appeared, which were in good agreement with those reported by Karpinsky and Evseev [27]. All the peaks were indexed with the tetragonal HMS with MnSi_{1.73} (ICSD # 43059) and cubic MnSi (ICSD # 71830) phases. XRD results on SPSed samples are in good agreement with earlier reports [22,25,28,29]. Higher contents of Yb (more than 1.0%) resulted in inhomogeneous composites among the ones having high fraction of MnSi intermetallic phase; this is the reason why they were not used for further characterization.

Crystallite size, phase content and theoretical densities of compacted samples were obtained from the Rietveld refined curves and are reported in **Table 1**. All pellets are dense (more than 93%) and the crystallite size is in the range of 120–160 nm. SPS compaction has assisted for solid-state reaction to attain complete HMS phase (about 90%) phase. Furthermore, Yb-HMS NCs showed less MnSi phase and more densification as compared to pure HMS (as reported in **Table 1**) that is also favorable for improved TE properties.

SEM micrographs elucidated the morphology and grain size; results from BM sample, SPS compacted pure HMS and Yb-HMS NCs are displayed in **Fig. 3(a-d)**, respectively. BM nanopowder shows inhomogeneous morphology with some agglomeration, that is attributed to the wet milling process, and particle size in the range of 50–500 nm, as shown in **Fig. 3(a)**. Fractured surfaces of SPS compacted samples from pure HMS, 0.5% and 1% Yb-HMS NCs are presented in **Fig. 3(b-d)**. Fractured surfaces revealed that most of the grains are below 500 nm and very little porosity was observed in compacted samples. However, we observed

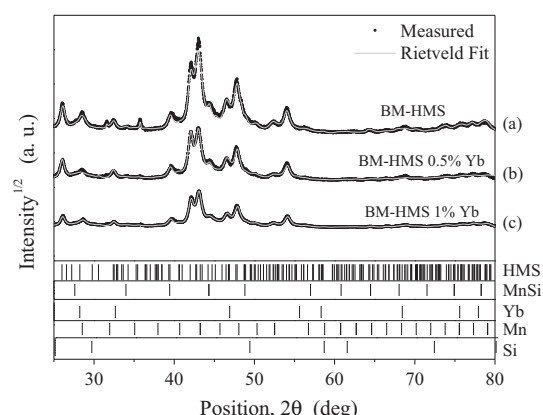


Fig. 1. XRD pattern of BM powders (a) HMS pure, (b) HMS with 0.5% Yb inclusion, (c) HMS with 1% Yb inclusion.

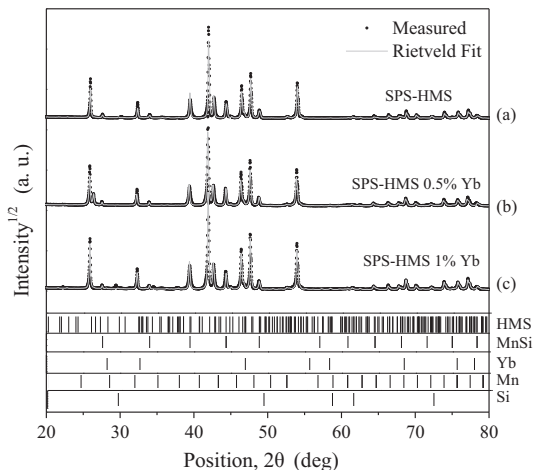


Fig. 2. XRD pattern of SPSed samples (a) HMS pure, (b) HMS with 0.5% Yb inclusion, (c) HMS with 1% Yb inclusion.

non-uniform dispersion of small entities at the grain boundaries, which may correspond to Yb inclusions. Zamanipour and co-workers have reported similar grain size after SPS compactions while Chen et al. presented effective grain growth after the hot press compaction [30,31]. However, high heating rate in SPS can overcome this challenge and grain growth can be minimized.

Transmission electron microscopy (TEM) was used to study the morphology evolution during the BM step. Fig. 4(a) displays a low-magnification TEM image, of the intermediate product with near-spherical morphology and clusters of small and large crystals. High resolution TEM (HRTEM) images were taken to examine the individual grains of SPSed samples as shown in Fig. 4(b). It shows lattice fringes and crystal symmetry; lattice parameter in the selected grain was calculated as 5.51 Å, corresponding to $a = b$ in the tetragonal phase of HMS, which agrees well with earlier reports [32]. Furthermore, HRTEM was performed over different spots in the sample to investigate the details of different grains; results are presented in Fig. S2.

Bright and dark field images were obtained with help of scanning transmission electron microscopy (STEM) and results are displayed in Fig. 5(a and b). HMS grains are clearly observed in the range of 300–500 nm, nevertheless there are grains below

Table 1
Rietveld refinement analysis results of HMS and Yb–HMS NCs.

Sample ID	Phase content		Crystallite size (HMS) (nm)	Geometrical density (g/cm ³)	Theoretical density (g/cm ³)	Relative density (%)
	MnSi (%)	HMS (%)				
HMS pure	10	90	160	4.865	5.23	93
HMS + 0.5%Yb	8	92	120	4.917	5.22	94
HMS + 1.0%Yb	7	93	130	4.985	5.21	96

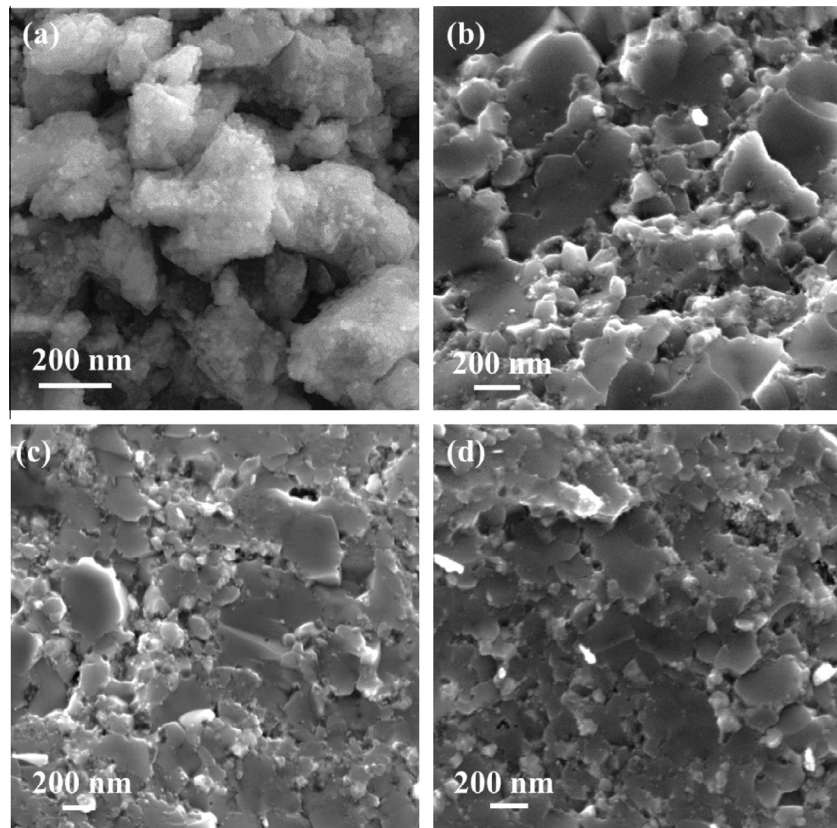


Fig. 3. SEM micrographs of: (a) HMS nanopowder after BM, (b) HMS after SPS compaction, (c) 0.5% Yb–HMS NC, (d) 1% Yb–HMS NC.

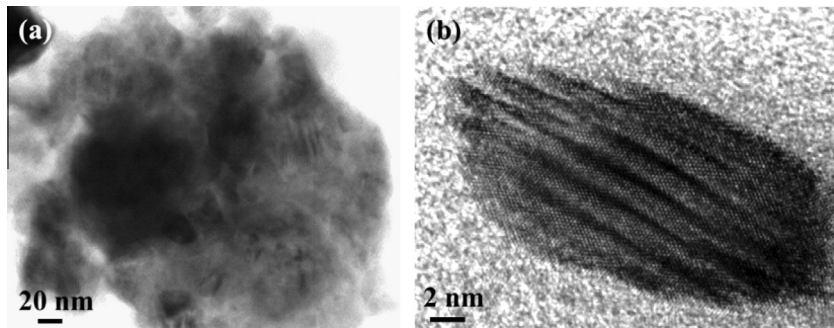


Fig. 4. TEM micrographs from BM pure HMS samples; (a) Lower and (b) Higher; magnifications.

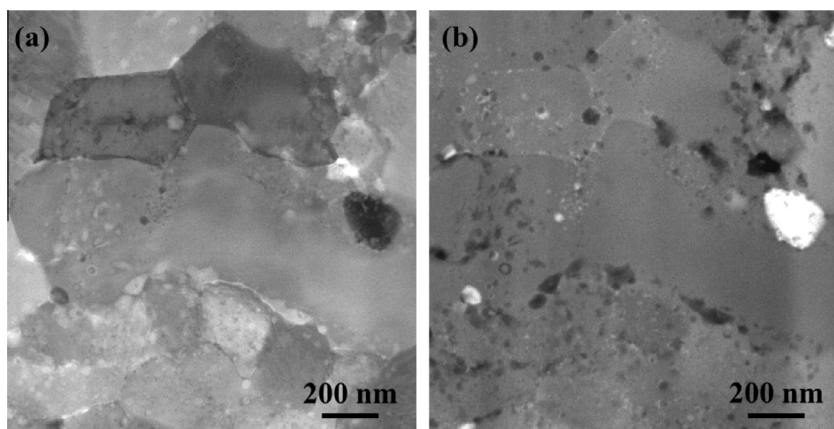


Fig. 5. STEM micrographs of 1% Yb-HMS NCs; (a) Bright field image, (b) dark field image.

200 nm. Dark grey color in bright field and white spots in dark field image represents Yb. Furthermore, it was observed in the later EDS mapping how this color contrast matches. Few other dark spots in Fig. 5(b) may represent other phases in the sample and few grains of light grey color reveal MnSi metallic phase, while most of the crystalline phase is HMS, as it is observed from the color contrast in both images. However, on the basis of microscopy observations, it is difficult to perform accurate quantitative analysis of MnSi grains due to varying crystal orientations. Also several regions show slightly different contrast, which means that the ratio Mn:Si is not constant, although the XRD identified pure HMS phase.

Fig. 6(a–c) shows EDS mapping analysis in the bulk sample, however, it is difficult to differentiate between HMS and MnSi phases in this type of analysis. In the elemental maps it is clearly observed that Yb inclusions are collected at the grain boundaries in the form of pinning points. Even smaller particles of Yb are dispersed overall in bulk NC as can be observed in Fig. 6(c–iii). However, some agglomerated grains of Yb was also detected which are in the range 50–100 nm. Elemental line profile for individual grains was also performed by TEM-EDS and the results are reported in Fig. S3.

The temperature dependent Seebeck coefficient (S) and the electrical resistivity (ρ) for pure HMS and Yb-HMS NCs are reported in the Fig. 7(a and b) respectively. All samples exhibit degenerate semiconductor behavior as the S and ρ increases with increasing temperature. Similar characteristics in HMS samples were observed and reported also by other research groups [33]. The positive sign of S confirms primarily p-type conduction mechanism. Yb inclusion in HMS samples have slightly affected the Seebeck values, such as 1% Yb-HMS NC increased the value from 90 to 185 $\mu\text{V}/\text{K}$. Norouzzadeh et al. predicted similar values of S from a theoretical model while assuming the grain size of 20 nm [33].

Sadia et al. reported lower S values (75–125 $\mu\text{V}/\text{K}$) of BM and SPSed HMS sample, which has been attributed to the higher amount of metallic phase of MnSi [25]. Electrical resistivity (ρ) in Yb-HMS NCs revealed significant influence of Yb, decreasing roughly to half of the value (2.25 $\text{m}\Omega\cdot\text{cm}$ @ 500 °C) in 1% Yb-HMS NC as compared to pure HMS compacted sample that display 3.35 $\text{m}\Omega\cdot\text{cm}$ at 500 °C, as shown in Fig. 7(b). We attributed this improvement to the presence of metallic (Yb) inclusions at the grain boundaries which were clearly observed in detailed TEM investigations. Pure HMS compacted samples contains similar ρ values as reported by various reports [20,25]. Carrier concentration (n_H) was also measured at 300 K by using the Hall measurement setup and the results are reported in Table 2. Pure HMS compacted sample have higher carrier concentration ($1.56 * 10^{21} \text{ cm}^{-3}$) as compared to 0.5% Yb NC ($1.16 * 10^{21} \text{ cm}^{-3}$). This discrepancy might be due to the inhomogeneous dispersion of Yb in the sample and it is difficult to estimate the accurate reason for such deviation. Though, 1% Yb-HMS NC has $1.75 * 10^{21} \text{ cm}^{-3}$ n_H value, which caused to increase the carrier mobility, hence improved the electrical conduction. Zhou et al. measured and reported $n_H = 1.50 * 10^{21} \text{ cm}^{-3}$ for pure HMS SPSed sample which is comparable to our results. However, in their case, addition of Ge increased n_H to $1.89 * 10^{21} \text{ cm}^{-3}$ whereas in our samples, 1% Yb-HMS NC reached a value of $1.75 * 10^{21} \text{ cm}^{-3}$.

Total thermal conductivity (κ) in all samples has relatively low values as compared to the bulk, measured κ values are in the range 2.6–3.2 W/mK in temperature range of 25–600 °C. MnSi_{1.73} prepared by melting, annealing and hot press exhibited κ values from 2.5 W/mK to 3 W/mK [34]. Sadia et al. reported higher κ values (about 4.5 W/mK) for MnSi_{1.73} prepared by BM for 5 hours at 800 rpm, though it was attributed to high MnSi content [25]. Yb-HMS NCs show slight decrease in total κ value, which confirms

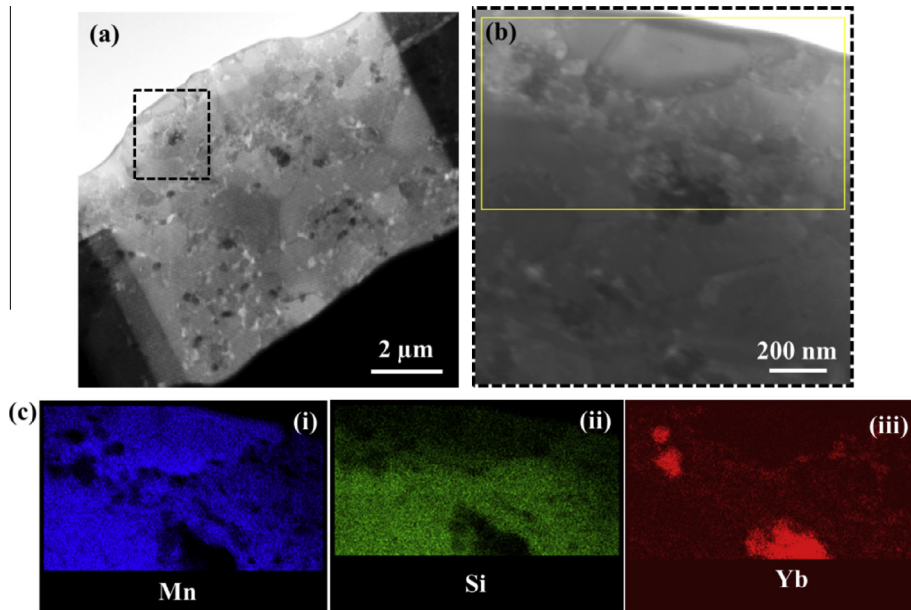


Fig. 6. (a) Low magnification, and (b) Selected area TEM micrographs for mapping; (c) EDS Mapping of 1% Yb-HMS NCs; (i) Manganese, (ii) silicon, (iii) Ytterbium.

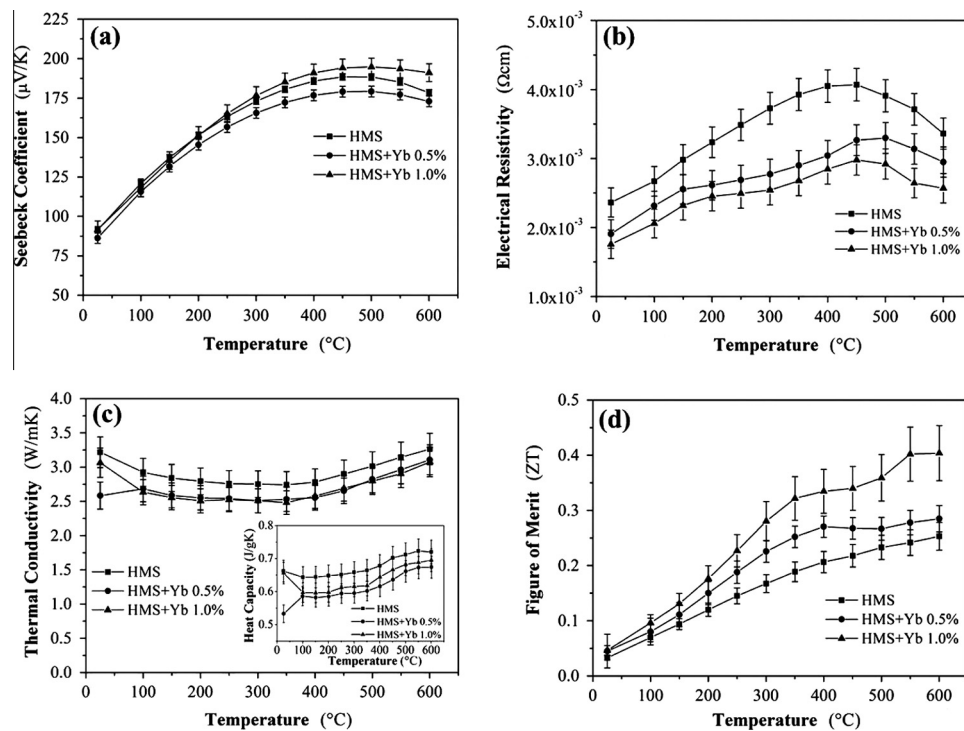


Fig. 7. Thermoelectric evaluation of compacted HMS samples; (a) Seebeck coefficient, (b) electrical resistivity, (c) thermal conductivity (inset heat capacity), and (d) figure of merit, ZT .

Table 2
Carrier concentration of HMS and Yb inclusion samples at 300 K.

Sample ID	Carrier concentration n_H ($\times 10^{21} \text{ cm}^{-3}$)
HMS pure	1.56
HMS + 0.5%Yb	1.16
HMS + 1.0%Yb	1.75

the phonon interactions at the grain boundaries. Furthermore, Yb composites have lower calculated crystallite size that might have

influenced the κ value. For NC samples, this decrease in total κ is also due to the decrease in MnSi phase content (as reported in Table 1). In the literature, other compositions of HMS such as $\text{MnSi}_{1.71}$ and $\text{MnSi}_{1.75}$ have shown lower values of total κ , for instance in the range of 1.5–2.5 W/mK [14]. Lattice thermal conductivity results confirm the major contribution in the total κ (results are reported in supplementary document in Fig. S4). The dimensionless figure of merit (ZT) is plotted in Fig. 7(d), which shows better performance of Yb-HMS NCs. ZT values of our pure HMS bulk sample is comparatively lower than reported by Luo

et al. [19] and Zhou et al. [35] the primary reason for this difference is the higher κ of our samples which is strongly related to the amount of MnSi phase in the compacted samples. Similar results were reported on BM and SPSed compacted sample which have similar high amount of MnSi as secondary phase [25]. HMS NCs show better performance while reaching the maximum ZT value to 0.42 @ 600 °C which is mainly affected due to the decrease in electrical resistivity. ZT value of these samples can be further improved by reducing the MnSi phase to reduce κ further.

4. Conclusions

Nanostructured HMS with $MnSi_{1.73}$ nominal composition and Yb–HMS NCs were prepared by ball milling from high purity elemental powders and SPS consolidation. Influence of Yb metal inclusions on the transport property of HMS was investigated. XRD patterns from the nanopowder and compacted samples allowed identification of various phases at different processing stages: bulk NCs have shown HMS as major phase though 7–10% MnSi phase was also detected that have affected the total κ as compared to earlier reports. SEM and HRTEM coupled with EDS analysis have been used to study the grain morphologies and elemental compositions in the bulk samples. EDS mapping revealed Yb inclusions at the grain boundaries. Electrical properties improved with larger amount of Yb while thermal conductivity decreased. ZT value of 1% Yb–HMS NC reached to the 0.42 @ 600 °C which is significantly higher as compared to pure HMS bulk sample. ZT further can be improved if the total κ reduces in the NCs with further reduction of the MnSi phase.

Acknowledgements

This research work has been funded by the Swedish Foundation for Strategic Research – SSF (EM11-0002), Swedish Energy Agency (36656-1), Stiftelsen of Richert J. Gust, and the Italian National Research Council – Italian Ministry of Economic Development Agreement “Ricerca di sistema elettrico nazionale”.

Appendix A. Supplementary material

Supplementary data associated with this article can be found, in the online version, at <http://dx.doi.org/10.1016/j.jallcom.2014.09.016>.

References

- [1] M. Martín-González, O. Caballero-Calero, P. Díaz-Chao, Nanoengineering thermoelectrics for 21st century: energy harvesting and other trends in the field, *Renew. Sustain. Energy Rev.* 24 (2013) 288–305, <http://dx.doi.org/10.1016/j.rser.2013.03.008>.
- [2] J.R. Sootsman, D.Y. Chung, M.G. Kanatzidis, New and old concepts in thermoelectric materials, *Angew. Chem. Int. Ed. Engl.* 48 (2009) 8616–8639, <http://dx.doi.org/10.1002/anie.200900598>.
- [3] M. Saleemi, M.S. Toprak, S. Li, M. Johnsson, M. Muhammed, Synthesis, processing, and thermoelectric properties of bulk nanostructured bismuth telluride (Bi_2Te_3), *J. Mater. Chem.* 22 (2012) 725, <http://dx.doi.org/10.1039/cjlm13880d>.
- [4] S. Battiston, S. Fiameni, M. Saleemi, S. Boldrini, A. Famengo, F. Agresti, et al., Synthesis and characterization of Al-Doped Mg_2Si thermoelectric materials, *J. Electron. Mater.* 42 (2013) 1956–1959, <http://dx.doi.org/10.1007/s11664-013-2482-6>.
- [5] S. Fiameni, A. Famengo, F. Agresti, S. Boldrini, S. Battiston, M. Saleemi, et al., Effect of synthesis and sintering conditions on the thermoelectric properties of n-doped Mg_2Si , *J. Electron. Mater.* (2014) 1–6, <http://dx.doi.org/10.1007/s11664-014-3048-y>.
- [6] S. Fiameni, A. Famengo, S. Boldrini, S. Battiston, M. Saleemi, M. Stingaci, et al., Introduction of metal oxides into Mg_2Si thermoelectric materials by spark plasma sintering, *J. Electron. Mater.* 42 (2013) 2062–2066, <http://dx.doi.org/10.1007/s11664-013-2522-2>.
- [7] M. Saleemi, M.S. Toprak, S. Fiameni, S. Boldrini, S. Battiston, A. Famengo, et al., Spark plasma sintering and thermoelectric evaluation of nanocrystalline magnesium silicide (Mg_2Si), *J. Mater. Sci.* 48 (2013) 1940–1946, <http://dx.doi.org/10.1007/s10853-012-6959-0>.
- [8] M. Toprak, Y. Zhang, M. Muhammed, Chemical alloying and characterization of nanocrystalline bismuth telluride, *Mater. Lett.* 57 (2003) 3976–3982, [http://dx.doi.org/10.1016/S0167-577X\(03\)00250-7](http://dx.doi.org/10.1016/S0167-577X(03)00250-7).
- [9] C. Stiewe, L. Bertini, M. Toprak, M. Christensen, D. Platzek, S. Williams, et al., Nanostructured $Co_{1-x}Ni_x(Sb_{1-y}Te_y)_3$ skutterudites: theoretical modeling, synthesis and thermoelectric properties, *J. Appl. Phys.* 97 (2005), <http://dx.doi.org/10.1063/1.1852072>.
- [10] A. Khan, M. Saleemi, M. Johnsson, L. Han, N.V. Nong, M. Muhammed, et al., Fabrication, spark plasma consolidation, and thermoelectric evaluation of nanostructured $CoSb_3$, *J. Alloys Comp.* 612 (2014) 293–300, <http://dx.doi.org/10.1016/j.jallcom.2014.05.119>.
- [11] H. Alam, S. Ramakrishna, A review on the enhancement of figure of merit from bulk to nano-thermoelectric materials, *Nano Energy* 2 (2013) 190–212, <http://dx.doi.org/10.1016/j.nanoen.2012.10.005>.
- [12] Y. Sadia, Y. Gelstein, Silicon-rich higher manganese silicides for thermoelectric applications, *J. Electron. Mater.* 41 (2012) 1504–1508, <http://dx.doi.org/10.1007/s11664-012-1936-6>.
- [13] L.D. Ivanova, Preparation of thermoelectric materials based on higher manganese silicide, *Inorg. Mater.* 47 (2011) 965–970, <http://dx.doi.org/10.1134/S002016851109010X>.
- [14] J. Higgins, A. Schmitt, Higher manganese silicide nanowires of nowotny chimney ladder phase, *J. Am. Chem. Soc.* (2008) 16086–16094, <http://dx.doi.org/10.1021/ja806512z>.
- [15] V.G. Zwilling, N. Aus, Zur Struktur der Defekt-Mangansilicide, *Chem. Mon.* 675 (1973) 668–675.
- [16] Y. Gelstein, J. Tunbridge, R. Dixon, M.J. Reece, H. Ning, R. Gilchrist, et al., Physical, mechanical, and structural properties of highly efficient nanostructured n- and p-silicides for practical thermoelectric applications, *J. Electron. Mater.* (2013), <http://dx.doi.org/10.1007/s11664-013-2848-9>.
- [17] N. Satyala, P. Norouzzadeh, D. Vashaee, *Nanoscale Thermoelectrics*, Springer International Publishing, Cham, 2014. doi: 10.1007/978-3-319-02012-9.
- [18] T. Yamada, Y. Miyazaki, H. Yamane, Preparation of Higher Manganese Silicide (HMS) bulk and Fe-containing HMS bulk using a Na–Si Melt and their thermoelectrical properties, *Thin Solid Films* 519 (2011) 8524–8527, <http://dx.doi.org/10.1016/j.tsf.2011.05.032>.
- [19] W. Luo, H. Li, F. Fu, W. Hao, X. Tang, Improved thermoelectric properties of Al-doped higher manganese silicide prepared by a rapid solidification method, *J. Electron. Mater.* 40 (2011) 1233–1237, <http://dx.doi.org/10.1007/s11664-011-1612-2>.
- [20] V. Ponnambalam, D.T. Morelli, S. Bhattacharya, T.M. Tritt, The role of simultaneous substitution of Cr and Ru on the thermoelectric properties of defect manganese silicides $MnSi_\delta$ ($1.73 < \delta < 1.75$), *J. Alloys Comp.* 580 (2013) 598–603, <http://dx.doi.org/10.1016/j.jallcom.2013.07.136>.
- [21] S. Ballikaya, N. Uzar, S. Yıldırım, J.R. Salvador, C. Uher, Journal of solid state chemistry high thermoelectric performance of In, Yb, Ce multiple filled $CoSb_3$ based skutterudite compounds, *J. Solid State Chem.* 193 (2012) 31–35, <http://dx.doi.org/10.1016/j.jssc.2012.03.029>.
- [22] A. Famengo, S. Battiston, M. Saleemi, S. Boldrini, S. Fiameni, F. Agresti, et al., Phase content influence on thermoelectric properties of manganese silicide-based materials for middle-high temperatures, *J. Electron. Mater.* 42 (2013) 2020–2024, <http://dx.doi.org/10.1007/s11664-013-2507-1>.
- [23] S. Boldrini, A. Famengo, F. Montagner, S. Battiston, S. Fiameni, M. Fabrizio, et al., Test rig for high-temperature thermopower and electrical conductivity measurements, *J. Electron. Mater.* 42 (2013) 1319–1323, <http://dx.doi.org/10.1007/s11664-012-2437-3>.
- [24] D.-K. Shin, K.-W. Jang, S.-C. Ur, I.-H. Kim, Thermoelectric properties of higher manganese silicides prepared by mechanical alloying and hot pressing, *J. Electron. Mater.* 42 (2013) 1756–1761, <http://dx.doi.org/10.1007/s11664-012-2415-9>.
- [25] Y. Sadia, L. Dinnerman, Y. Gelstein, Mechanical alloying and spark plasma sintering of higher manganese silicides for thermoelectric applications, *J. Electron. Mater.* 42 (2013) 1926–1931, <http://dx.doi.org/10.1007/s11664-013-2476-4>.
- [26] A. Allam, P. Boulet, C.A. Nunes, J. Sopousek, P. Broz, M.-C. Record, Phase transformations in higher manganese silicides, *J. Alloys Comp.* 551 (2013) 30–36, <http://dx.doi.org/10.1016/j.jallcom.2012.10.016>.
- [27] G.O. Karpinsky, B.A. Evseev, Crystal structure of Mn_4Si_7 , *Izv. AN SSSR Neorg. Mater.* 5 (1969) 525–534.
- [28] T. Itoh, M. Yamada, Synthesis of thermoelectric manganese silicide by mechanical alloying and pulse discharge sintering, *J. Electron. Mater.* 38 (2009) 925–929, <http://dx.doi.org/10.1007/s11664-009-0697-3>.
- [29] Y.-J. Shi, Q.-M. Lu, X. Zhang, J.-X. Zhang, Microstructure and thermoelectric properties of higher manganese silicides, *J. Inorg. Mater.* 26 (2011) 691–695, <http://dx.doi.org/10.3724/SP.J.1072.2011.00691>.
- [30] X. Chen, A. Weathers, A. Moore, J. Zhou, L. Shi, Thermoelectric properties of cold-pressed higher manganese silicides for waste heat recovery, *J. Electron. Mater.* 41 (2012) 1564–1572, <http://dx.doi.org/10.1007/s11664-012-1987-8>.
- [31] Z. Zamanipour, X. Shi, M. Mozafari, J.S. Krasinski, L. Tayebi, D. Vashaee, Synthesis, characterization, and thermoelectric properties of nanostructured bulk p-type $MnSi_{1.73}$, $MnSi_{1.75}$, and $MnSi_{1.77}$, *Ceram. Int.* 39 (2013) 2353–2358, <http://dx.doi.org/10.1016/j.ceramint.2012.08.086>.

- [32] E.I. Suvorova, V.V. Klechkovskaya, Precipitates of MnSi cubic phase in tetragonal Mn₄Si₇ crystal, *Crystallogr. Rep.* 58 (2013) 854–861, <http://dx.doi.org/10.1134/S1063774513060229>.
- [33] P. Norouzzadeh, Z. Zamanipour, J.S. Krasinski, D. Vashaee, The effect of nanostructuring on thermoelectric transport properties of p-type higher manganese silicide MnSi_{1.73}, *J. Appl. Phys.* 112 (2012) 124308, <http://dx.doi.org/10.1063/1.4769884>.
- [34] E. Grob, M. Riffel, U. Stohrer, Thermoelectric generators made of FeSi₂ and HMS: fabrication and measurement, *J. Mater. Res.* 10 (1995).
- [35] A.J. Zhou, T.J. Zhu, X.B. Zhao, S.H. Yang, T. Dasgupta, C. Stiewe, et al., Improved thermoelectric performance of higher manganese silicides with Ge additions, *J. Electron. Mater.* 39 (2009) 2002–2007, <http://dx.doi.org/10.1007/s11664-009-1034-6>.